DTU Library

Estimations of Interlayer Contacts in Extrusion Additive Manufacturing Using a CFD Model

Comminal, Raphaël; Jafarzadeh, Sina; Serdeczny, Marcin; Spangenberg, Jon

Published in:
Industrializing Additive Manufacturing

Link to article, DOI:
10.1007/978-3-030-54334-1_17

Publication date:
2020

Document Version
Peer reviewed version

Citation (APA):
Comminal, R., Jafarzadeh, S., Serdeczny, M., & Spangenberg, J. (2020). Estimations of Interlayer Contacts in Extrusion Additive Manufacturing Using a CFD Model. In M. Meboldt, & C. Klahn (Eds.), *Industrializing Additive Manufacturing: Proceedings of AMPA 2020* Springer. https://doi.org/10.1007/978-3-030-54334-1_17

Estimations of interlayer contacts in extrusion additive manufacturing using a CFD model

Raphaël Comminal*[0000-0003-3764-5550], Sina Jafarzadeh[0000-0002-1645-7705], Marcin P. Serdeczny[0000-0003-1691-773X], and Jon Spangenberg[0000-0002-5411-6821]

Department of Mechanical Engineering, Technical University of Denmark, 2800 Kgs. Lyngby, Denmark

* rcom@mek.dtu.dk

Abstract. Numerical modeling is one of the key components in the development of digital twins of Additive Manufacturing (AM) processes, encompassed in the concept of Industry 4.0. Numerical simulations also have a role to play in the improvement of contemporary AM techniques, among which material extrusion is very popular. Computational Fluid Dynamics (CFD) models have recently proven successful for simulating the deposition flow in extrusion AM. Previous modeling works using CFD have been able to predict the influence of processing parameters on the cross-sectional shape of the printed strand, as well as the mesostructure formation resulting from their deposition and fusing. The present study focuses on using CFD simulations to quantify the waviness of a strand extruded on top of a previous layer with an orthogonal print direction, which often occurs when printing a part with a rectilinear infill pattern and alternate 0°/90° raster angles from layer to layer. The variations in the strand width and thickness of the second layer were found to depend on the strand-to-strand gap in the first layer. The CFD model was also used to determine the interlayer penetration depth, which enhances mechanical performances.

Keywords: Numerical simulations, Material extrusion additive manufacturing, Computational fluid dynamics, Deposition flow, Interlayer contact.

1 Introduction

Material extrusion is one of the prominent techniques used for Additive Manufacturing (AM). The concept of material extrusion AM consists in depositing a continuous strand of material along a computer-generated toolpath, to build a part layer by layer. It has successfully been applied with a broad range of materials, including several types of plastics (thermoplastics, thermosets and rubber), hydrogels, ceramic pastes, molten metals, concrete, etc. Depending on the material, different extrusion technologies have been used: filament-fed extrusion, screw extruder, syringe extruder, and hydraulic pump.

Some of the current challenges with material extrusion AM include the improvement of the geometrical conformity (dimensional tolerance and surface quality) and mechanical properties of the manufactured components. Generally, the parts manufactured by material extrusion AM have porosities, and that reduces their mechanical performances when compared to the equivalent parts manufactured by conventional methods (e.g. injection molding) [1-3]. The porosity directly depends on the mesostructure formed by the successive deposition of the strands, which is influenced by the printing parameters [4]. Moreover, the mechanical properties of the component are intrinsically linked to the inter- and intra-layer bonds in the mesostructure [5-8].

A voxelized model of material deposition that is solely based on volume conservation was developed by Gleadall et al. [9] to predict the micro-architectures of 3D printed scaffolds. A detailed flow analysis of material spreading during extrusion AM was proposed in [10]. Computational Fluid Dynamics (CFD) simulations have been used in [11-22] to model the deposition of strands. Du et al. [11] used CFD to analyze the thermal field and morphology of a 3D printed thin wall of ABS. Comminal et al. [12] employed an isothermal Newtonian creeping flow model to investigate the influence of the printing parameters on the cross-sectional shape of the strand deposited on a planar surface. The numerical predictions of the model were later validated through experimental measurements by Serdeczny et al. [13]. In a complementary study, the same team [14] used a power-law shear-shinning model and showed that the numerical results were insensitive to the rheological model, confirming that the Newtonian creeping flow assumption was a valid modeling hypothesis. The corner rounding and swelling at turns was also modeled by Comminal et al. [15, 16]. Xia et al. [17-20] simulated the deposition of multiple strands and layers, with a non-isothermal and non-Newtonian fluid flow model. In their model, the deposited strands have the possibility to deform under the pressure applied by the layers deposited on top of them. Several cases were simulated, included the multi-layer deposition of parallel and orthogonal strands. In contrast, Serdeczny et al. [21, 22] modeled the multi-layer deposition of parallel strands with an isothermal Newtonian creeping flow model. Moreover, the mesostructure formation was simulated by successive simulations where the previously deposited strands were treated as solid bodies excluded from the flow domain. The cases of aligned and skewed layers of parallel strands were considered. These simulations estimated the porosity, surface roughness, and inter-/intra- layer contact areas, and agreed qualitatively well with the experimental results.

The current work presents novel numerical analysis of the strand deposition on top of a previous layer with an orthogonal print direction. This situation frequently occurs when printing a part with a rectilinear infill pattern and alternate 0°/90° raster angles from layer to layer. The numerical model is applied to investigate the influence of the distance between the strands of the first layer on the waviness of the second layer, as well as the interlayer penetration depth.

2 Numerical methods

This work uses the same modeling assumptions as in the previous works of Comminal et al. [12, 16] and Serdeczny et al. [13, 22], but the numerical solutions are obtained with a different numerical scheme, using the CFD software ***FLOW-3D***® [23]. The flow is modeled as an isothermal Newtonian fluid flow, which is governed by the continuity equation and the momentum conservation equation:

$$\nabla \cdot \boldsymbol{u} = 0 \tag{1}$$

$$\rho \left(\frac{\partial \boldsymbol{u}}{\partial t} + \boldsymbol{u} \cdot \nabla \boldsymbol{u} \right) = -\nabla p + \eta \nabla^2 \boldsymbol{u} + \rho \boldsymbol{g} \tag{2}$$

where $\boldsymbol{u}$ is the velocity vector field, p is the pressure, ρ is the material density, η is the dynamic viscosity, $\boldsymbol{g}$ is the gravity acceleration vector, and t is the time. The following material parameters, $\rho = 1000$ kg/m^3 and $\eta = 1000$ Pa·s were used. As discussed in [12, 13], the extrusion flow typically has a very low Reynolds number $Re \sim 10^{-3}$, corresponding to the creeping flow regime. This means that the flow is virtually insensitive to the material density and viscosity – as long as $Re = \rho UD/\eta << 1$, where U and D are the characteristic speed and characteristic length of the flow, respectively (e.g. the extrusion speed and the nozzle diameter). For that reason, the temperature-variation of the viscosity is neglected, and the flow is solved as isothermal.

The material deposition was simulated inside a build volume of 5.6 × 1.1 × 2.0 mm, along the X-Y-Z directions. The build volume contains the extrusion nozzle and the substrate, which are both included as solid objects into the computational domain, as shown in Figure 1. The geometry of the extrusion nozzle is a cylindrical tube with an inner diameter $D = 0.4$ mm and a wall thickness of 0.25 mm. In addition, the top boundary of the computational domain was covered by an upper plate with a hole coinciding with the nozzle orifice. The substrate comprises a planar build surface and one layer of parallel strands, previously printed on that surface. Six different strand configurations of the first layer were used in the simulations. The different geometries of the first layer were generated by duplicating the geometry of a single strand, obtained from a previous numerical simulation of strand deposition [13] (case $g/D = 0.8$ and $V/U = 1.0$). All the substrate geometries have the same layer thickness $T_1 = 0.30$ mm (obtained for a nozzle height $H_1 = 0.32$ mm), but different strand repetition distances S, varying from 0.4 to 1.6 mm. The 3D geometries of the first layer were extruded through the computational domain along the Y direction. For the deposition simulations of the second layer, the nozzle was positioned at the distance $H_2 = 2H_1 = 0.64$ mm above the build plane.

During the simulations, the extrusion nozzle moved along the X direction inside the computational domain (thus a 90° raster angle with the first layer), with a constant travel speed $V = 20$ mm/s, while extruding material (in the Z direction) with a steady volumetric flux $U = 20$ mm/s. The same values of the nozzle travel speed and extrusion rate were used in [13] to simulate the deposition of the strand constituting the first layer. Note that the upper plate (that moves together with the nozzle) is used for restricting the material inlet to the nozzle, as the inflow boundary condition was applied to the entire top surface of the computational domain. The computational cost was reduced by placing a symmetry boundary condition on the transversal X-Z plane passing through the axis of the nozzle. Thus, the actual computational domain included only half of the nozzle geometry, and was 5.6 × 0.55 × 2.0 mm. A continuative outlet boundary condition was applied at the other boundaries of the computational domain. Moreover, the no-slip boundary condition was applied to the surface of all solid objects.

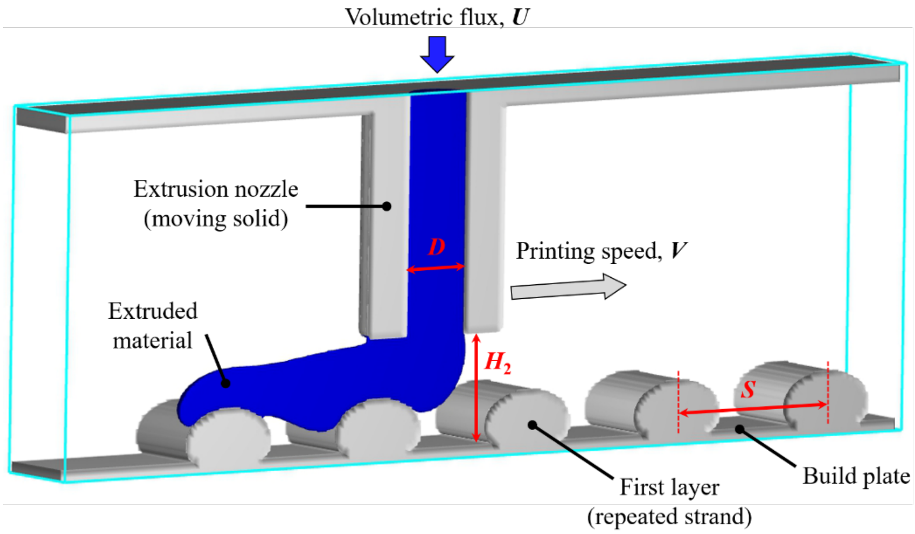

Fig. 1. Geometry of the CFD simulations. Computational domain delimited by the cyan box. The front plane is a symmetry boundary.

The computational domain was meshed with a Cartesian grid that has a uniform grid size of 20 μm. The governing equations of the flow were discretized with the finite volume method. The partial blockage of the grid cells by the solid objects (i.e. the moving nozzle and substrate) was taken into account with the immersed boundary method. In addition, the free surface of the extruded material was captured with the volume-of-fluid method. The simulations used a single-phase solver that only resolved the flow of extruded material, and neglected the surrounding air (in contrast with the previous works [12-16, 21, 22]). An adaptive time step size was used and the total simulation time was 0.27 s.

3 Numerical results

Snapshots of the extruded strand at different time points of the simulations are shown in Figure 2, where S = 1.0 mm. The final shapes of the extruded strands in the other simulations with different strand repetition distances S are also represented in Figure 3. The strand of the second layer presents a wavy shape, which contrasts with the strands of the first layer (deposited on a planar surface) that have a uniform width W_1 and thickness T_1; see Figure 4. The width W_2 and thickness T_2 of the second layer strand are functions of the position along the strand, as shown in Figure 4. The strand thickness T_2, corresponds the distance between the top of the first layer (represented by the dashed red line in Figure 4b) and the highest point of the free surface of the second layer strand.

The variations in the strand size has the same periodicity as the strand repetition distance. The minimum strand width $W_{2,min}$ is located at the middle of the gaps between the strands of the first layer, while the maximum strand width $W_{2,max}$ occurs on top of the first layer strands, where the nozzle-to-substrate distance is the lowest. When moving along the second layer strand in the same direction as the printing head, the lowest strand thickness $T_{2,\min}$ occurs at the end of every strands in the first layer (i.e. the beginning of the strand-to-strand gap). Moreover, the largest strand thickness $T_{2,\max}$ is located at the beginning of each strand in the first layer (i.e. the end of the strand-to-strand gap).

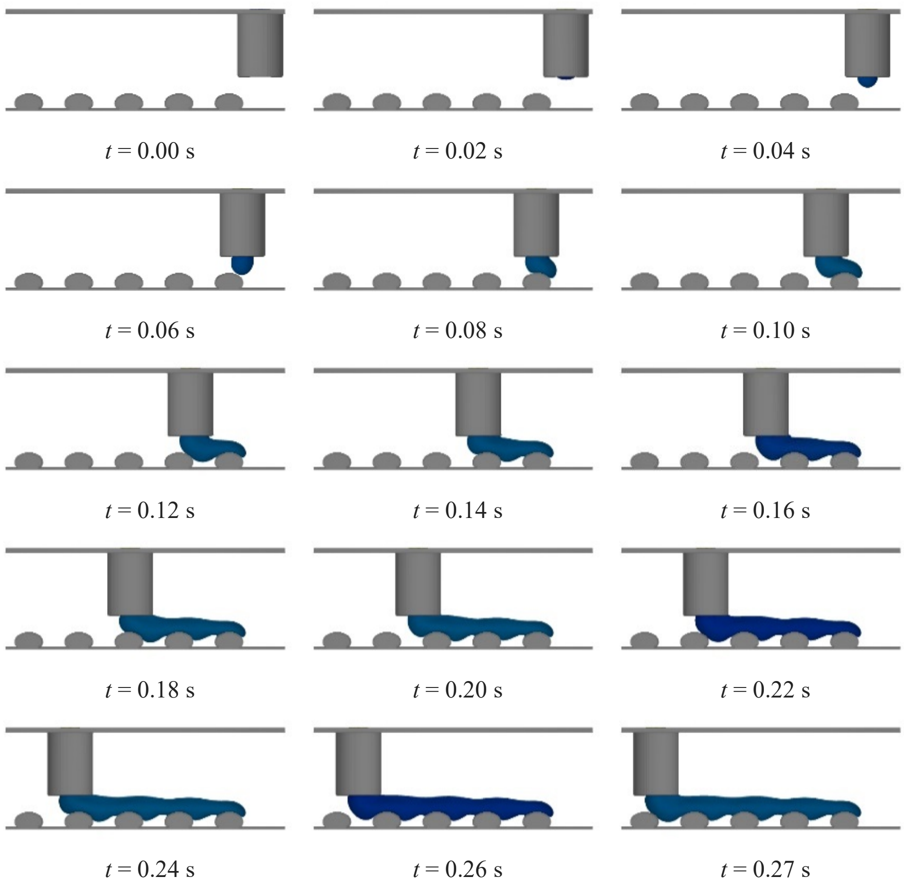

Fig. 2. Free surface of second layer strand, printed on top of a first layer with a strand repetition distance $S = 1.0$ mm. Snapshot every 0.02 s and at the final simulation time ($t = 0.27$ s).

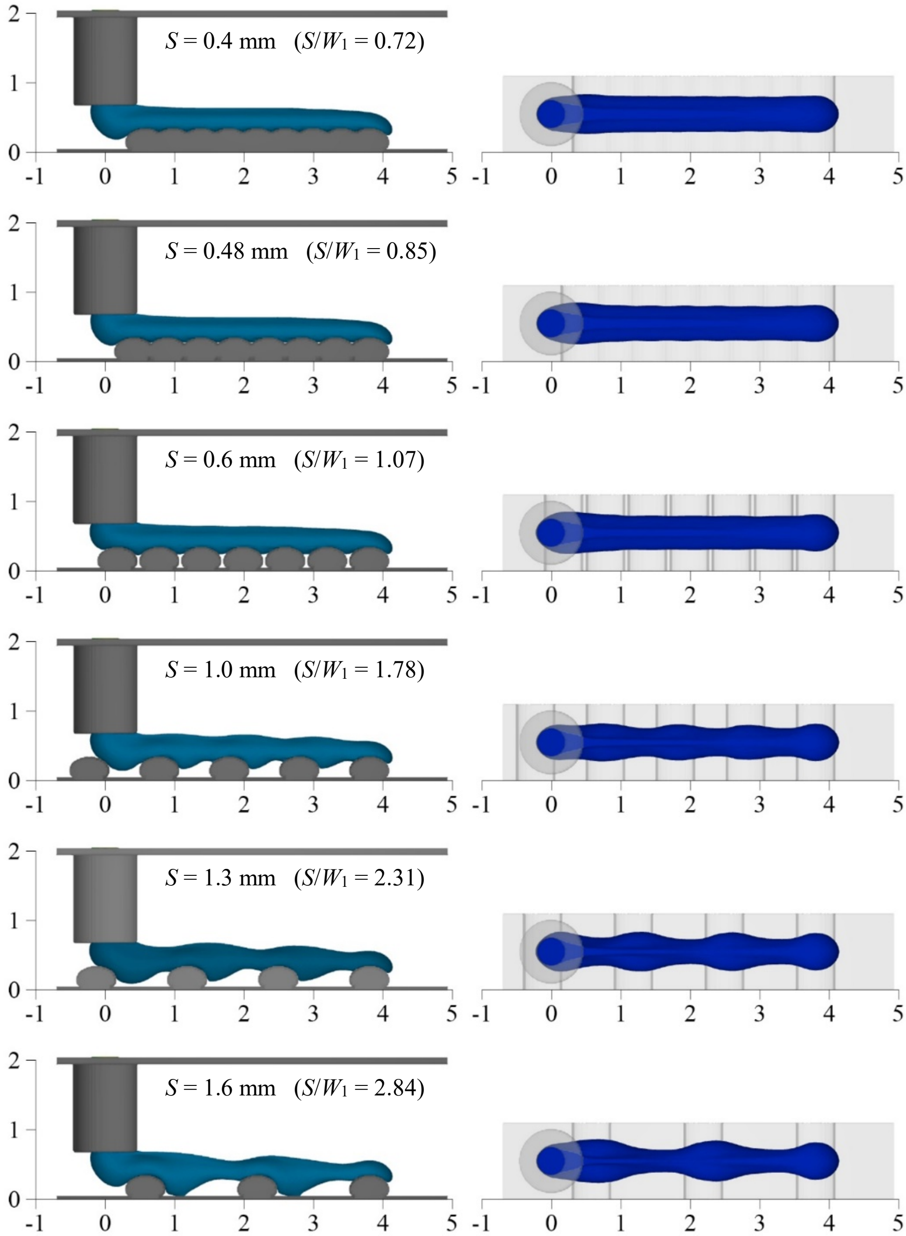

Fig. 3. Side and top views of the strand at the final simulation time, for different strand repetition distance S of the first layer. Axis units are in mm.

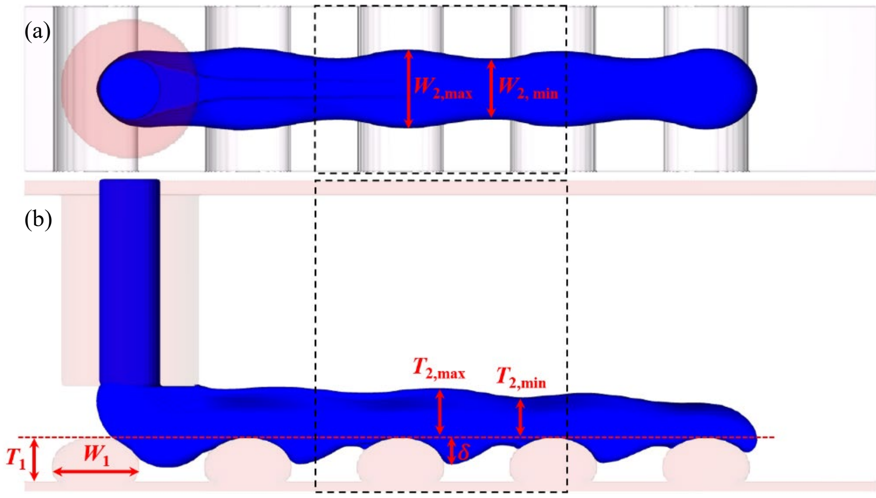

Fig. 4. Definitions of the strand dimensions. Top view (a) and side view (b). The red dashed line represents the top of the first layer. The black dashed lines show the measuring region.

The maximum and minimum values of the strand width and thickness of the second layer are plotted as a function of the strand repetition distance of the first layer in Figure 5. To avoid the end effects of extrusion starting and finishing, the dimensions of the strand were only measured within the central region of the simulation domain, represented by the black dashed lines in Figure 4. For ease of comparison, the dimensions of the first layer strands are also represented by the blue dashed lines in Figure 5. It should be noted that the strand dimensions reported in Figure 5 are normalized by the nozzle diameter ($D = 0.4$ mm), while the strand repetition distances are normalized by the first layer strand width ($W_1 = 0.56$ mm). The results show that the waviness (i.e. the difference between the maximum and minimum dimensions) of the second layer strand remains limited when $S/W_1 < 1$. This is explained by the fact that the overlap in the first layer strands makes the first layer closer to a flat surface. However, when $S/W_1 > 1$, the waviness tends to increase with the strand-to-strand gap (i.e. the strand repetition distance) in the first layer.

The interlayer penetration depth δ (defined as the distance between the top surface of the first layer and the lowest point of the second layer, see Figure 4b) is reported in Figure 6. The interlayer penetration depth is normalized by the thickness of the first layer ($T_1 = 0.30$ mm), and according to the numerical results, the interlayer penetration depth increases almost linearly with the strand repetition distance. Moreover, the maximum value $\delta/T_1 = 1$ is attained when the second layer completely collapses into the first layer and touches the build plate. This is visible in the case where $S/W_1 = 2.84$.

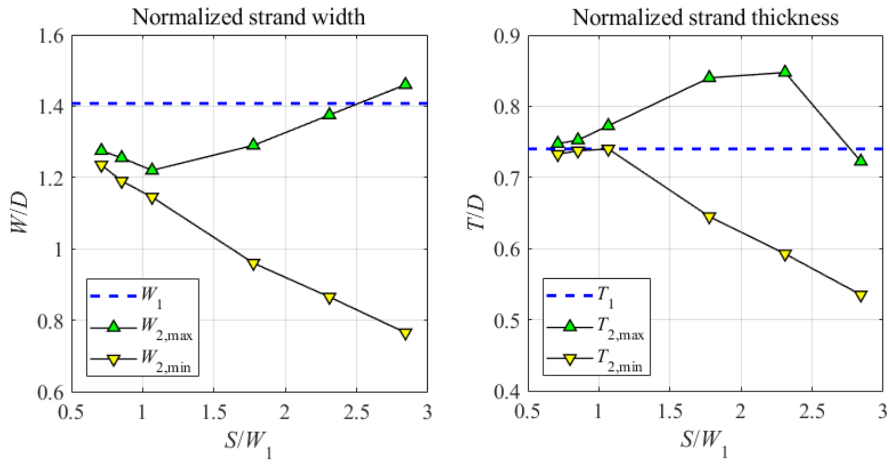

Fig. 5. Maximum and minimum normalized strand width W_2/D and thickness T_2/D as a function of the normalized strand repetition distance S/W_1 of the first layer.

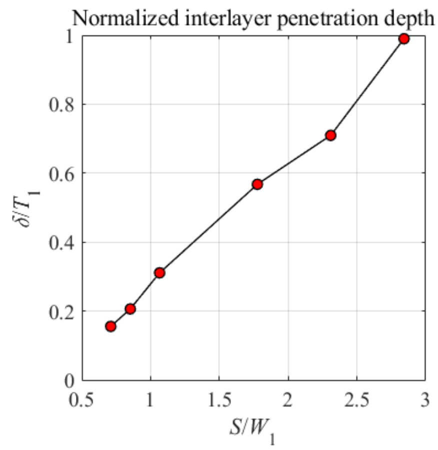

Fig. 6. Normalized interlayer penetration depth δ/T_1 as a function of the normalized strand repetition distance S/W_1 of the first layer.

4 Concluding remarks

This work presents a novel numerical simulation of the strand deposition on top of a previously printed layer of parallel strands with an orthogonal printing direction. The numerical model is based on the isothermal Newtonian creeping flow assumptions, which have proven sufficient in our previous works [12, 13, 16, 22], to investigate the influence of the printing parameters on the strand morphology and the mesostructure of 3D printed parts.

The mechanical strength of 3D printed parts depends on the contact area between the extruded strands, as well as the bonding strength of those contacts. The current CFD model does not predict the bonding strength of the interlayer contacts, which, in the case of thermoplastics, is a temperature-driven molecular diffusion process. Nevertheless, the isothermal CFD simulations provide information about interlayer contacts. The numerical results show that the maximum strand width of the second layer and the interlayer penetration depth – which both promote the interlayer contact between individual strands – increase with the strand repetition distance of the first layer. At the same time, however, the number of interlayer contacts per unit length of printed strand decreases with the strand repetition distance, which needs to be taken into account to evaluate the total interlayer contact area.

The main message of these numerical results is that printing layers with alternate printing directions from layer to layer can result in non-uniform strands. Future works should validate the simulated strand deformations with experiments. Finally, this type of numerical simulations could be useful for improving slicer software and exploring novel deposition strategies, toward more reliable and efficient material extrusion AM techniques.

Acknowledgments. The authors would like to acknowledge the support of the Danish Council for Independent Research (DFF), Technology and Production Sciences (FTP) (Contract No. 7017-00128).

References

1. Ahn, S. H., Montero, M., Odell, D., Roundy, S., Wright, P. K: Anisotropic material properties of fused deposition modeling ABS. Rapid prototyping journal 8(4), 248–257 (2002). https://doi.org/10.1108/13552540210441166
2. Koch, C., Van Hulle, L., Rudolph, N.: Investigation of mechanical anisotropy of the fused filament fabrication process via customized tool path generation. Additive Manufacturing 16, 138–145 (2017). https://doi.org/10.1016/j.addma.2017.06.003
3. Dawoud, M., Taha, I., Ebeid, S. J.: Mechanical behaviour of ABS: An experimental study using FDM and injection moulding techniques. Journal of Manufacturing Processes 21, 39–45 (2016). https://doi.org/10.1016/j.jmapro.2015.11.002
4. Rodriguez, J. F., Thomas, J. P., Renaud, J. E.: Characterization of the mesostructure of fused-deposition acrylonitrile-butadiene-styrene materials. Rapid Prototyping Journal 6(3), 175–186 (2000). https://doi.org/10.1108/13552540010337056
5. Rodríguez, J. F., Thomas, J. P., Renaud, J. E.: Mechanical behavior of acrylonitrile butadiene styrene fused deposition materials modeling. Rapid Prototyping Journal 9(4), 219–230 (2003). https://doi.org/10.1108/13552540310489604
6. Bellini, A., Güçeri, S.: Mechanical characterization of parts fabricated using fused deposition modeling. Rapid Prototyping Journal 9 (4), 252–264 (2003). https://doi.org/10.1108/13552540310489631
7. Ang, K. C., Leong, K. F., Chua, C. K., Chandrasekaran, M.: Investigation of the mechanical properties and porosity relationships in fused deposition modelling-fabricated porous structures. Rapid Prototyping Journal 12(2), 100–105 (2006). https://doi.org/10.1108/13552540610652447

8. Abbott, A. C., Tandon, G. P., Bradford, R. L., Koerner, H., Baur, J. W.: Process-structure-property effects on ABS bond strength in fused filament fabrication. Additive Manufacturing 19, 29–38 (2018). https://doi.org/10.1016/j.addma.2017.11.002
9. Gleadall, A., Ashcroft, I., Segal, J.: VOLCO: a predictive model for 3D printed microarchitecture. Additive Manufacturing 21, 605–618 (2018). https://doi.org/10.1016/j.addma.2018.04.004
10. Agassant, J. F., Pigeonneau, F., Sardo, L., Vincent, M.: Flow analysis of the polymer spreading during extrusion additive manufacturing. Additive Manufacturing 29, 100794 (2019). https://doi.org/10.1016/j.addma.2019.100794
11. Du, J., Wei, Z., Wang, X., Wang, J., Chen, Z.: An improved fused deposition modeling process for forming large-size thin-walled parts. Journal of Materials Processing Technology 234, 332–341 (2016). https://doi.org/10.1016/j.jmatprotec.2016.04.005
12. Comminal, R., Serdeczny, M. P., Pedersen, D. B., Spangenberg, J.: Numerical modeling of the strand deposition flow in extrusion-based additive manufacturing. Additive Manufacturing 20, 68–76 (2018). https://doi.org/10.1016/j.addma.2017.12.013
13. Serdeczny, M. P., Comminal, R., Pedersen, D. B., Spangenberg, J.: Experimental validation of a numerical model for the strand shape in material extrusion additive manufacturing. Additive Manufacturing 24, 145–153 (2018). https://doi.org/10.1016/j.addma.2018.09.022
14. Serdeczny, M. P., Comminal, R., Pedersen, D. B., Spangenberg, J.: Numerical study of the impact of shear thinning behaviour on the strand deposition flow in the extrusion-based additive manufacturing. In: Billington, D., Leach, R. K., Phillips, D., Riemer, O., Savio, E. (eds.) Proceedings of the 18th International Conference of the European Society for Precision Engineering and Nanotechnology, pp. 283–284. The European Society for Precision Engineering and Nanotechnology (2018).
15. Comminal, R., Serdeczny, M. P., Pedersen, D. B., Spangenberg, J.: Numerical modeling of the material deposition and contouring precision in fused deposition modeling. In: Proceedings of the 29th Annual International Solid Freeform Fabrication Symposium, pp. 1855–1864. Laboratory for Freeform Fabrication, Austin, TX (2018).
16. Comminal, R., Serdeczny, M. P., Pedersen, D. B., Spangenberg, J.: Motion planning and numerical simulation of material deposition at corners in extrusion additive manufacturing. Additive Manufacturing 29, 100753 (2019). https://doi.org/10.1016/j.addma.2019.06.005
17. Xia, H., Lu, J., Dabiri, S., Tryggvason, G.: Fully resolved numerical simulations of fused deposition modeling. Part I: fluid flow. Rapid Prototyping Journal 24(2), 463–476 (2018). https://doi.org/10.1108/RPJ-12-2016-0217
18. Xia, H., Lu, J., Tryggvason, G.: Fully resolved numerical simulations of fused deposition modeling. Part II–solidification, residual stresses and modeling of the nozzle. Rapid Prototyping Journal 24(6), 973–987 (2018). https://doi.org/10.1108/RPJ-11-2017-0233
19. Xia, H., Lu, J., Tryggvason, G.: Simulations of fused filament fabrication using a front tracking method. International Journal of Heat and Mass Transfer 138, 1310–1319 (2019). https://doi.org/10.1016/j.ijheatmasstransfer.2019.04.132
20. Xia, H., Lu, J., Tryggvason, G.: A numerical study of the effect of viscoelastic stresses in fused filament fabrication. Computer Methods in Applied Mechanics and Engineering 346, 242–259 (2019). https://doi.org/10.1016/j.cma.2018.11.031
21. Serdeczny, M. P., Comminal, R., Pedersen, D. B., Spangenberg, J.: Numerical prediction of the porosity of parts fabricated with fused deposition modeling. In: Proceedings of the 29th Annual International Solid Freeform Fabrication Symposium, pp. 1849–1854. Laboratory for Freeform Fabrication, Austin, TX (2018).

22. Serdeczny, M. P., Comminal, R., Pedersen, D. B., Spangenberg, J.: Numerical simulations of the mesostructure formation in material extrusion additive manufacturing. Additive Manufacturing 28, 419–429 (2019). https://doi.org/10.1016/j.addma.2019.05.024
23. Flow Science, Inc., Santa Fe, NM, FLOW-3D® Version 12.0 (2019).